BIOCHEMISTRY
including biophysical chemistry & molecular biology

Article

pubs.acs.org/biochemistry

P450cin Active Site Water: Implications for Substrate Binding and Solvent Accessibility

Yarrow Madrona, Scott A. Hollingsworth, Bushra Khan, and Thomas L. Poulos*

Departments of Molecular Biology and Biochemistry, Chemistry, and Pharmaceutical Sciences, University of California, Irvine, California 92697-3900, United States

Supporting Information

ABSTRACT: In P450cin, Tyr81, Asp241, Asn242, two water molecules, and the substrate participate in a complex H-bonded network. The role of this H-bonded network in substrate binding and catalysis has been probed by crystallography, spectroscopy, kinetics, isothermal titration calorimetry (ITC), and molecular dynamics. For the Y81F mutant, the substrate binds about 20-fold more weakly and V_{max} decreases by about 30% in comparison to WT. The enhanced susceptibility of the heme to H_2O_2-mediated destruction in Y81F suggests that this mutant favors the open, low-spin conformational state. Asn242 H-bonds directly with the substrate, and replacing this residue with Ala results in water taking the place of the missing Asn side chain. This mutant exhibits a 70% decrease in activity. Crystal structures and molecular dynamics simulations of substrate-bound complexes show that the solvent has more ready access to the active site, especially for the N242A mutant. This accounts for about a 64% uncoupling of electron transfer from substrate hydroxylation. These data indicate the importance of the interconnected water network on substrate binding and on the open/closed conformational equilibrium, which are both critically important for maintaining high-coupling efficiency.

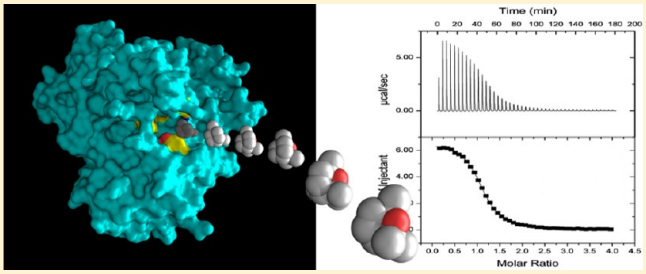

Cytochrome P450 enzymes (CYPs) catalyze the oxidation of a diverse range of compounds including xenobiotics, steroids, and, in some bacteria, compounds that are oxidatively assimilated as energy sources using the following reaction.

$$R{-}H + NADPH + O_2 + H^+ \rightarrow R{-}OH + NADP^+ + H_2O$$

NADPH or NADH provides two electrons that are sequentially transferred to the heme iron to activate molecular dioxygen and ultimately hydroxylate the subtrate. P450 enzymes exhibit varying levels of uncoupling, producing hydrogen peroxide or water instead of a hydroxylated product. However, tightly controlled P450 enzymes have precise water-mediated H-bonding networks that ensure proper dioxygen protonation. Disrupting this network can lead to the nonspecific delivery of protons that uncouple NADPH consumption from substrate hydroxylation. Much of the earlier proposals on the O_2-activation process were based on P450 structures in the so-called closed state. However, it is now clear that key elements of the O_2-activation machinery show much more conformational freedom than could be seen in the early substrate-bound crystal structures. A recent P450cam substrate-free structure[1] as well as the intermediate structures of substrate-analog tethered linkers[2] shows dynamic retractions of the F and G helices and B and C loops in the absence of substrate. The open/close transition has been also studied in solution using spectroscopic methods such as DEER[3] and NMR.[4] This kind of flexibility is likely to be important in oxygen activation in P450cam,[5,6] and we have postulated that similar motions are important when comparing the P450cin substrate-bound and substrate-free structures (Figure 1).[7]

P450cin is found in the soil bacterium *Citrobacter brakii* and shares many properties with P450cam and other bacterial

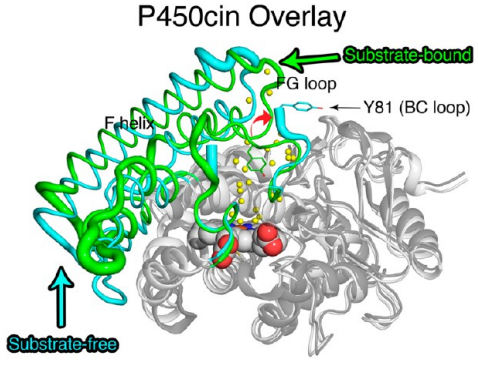

Figure 1. Overlay of substrate-free and substrate-bound P450cin. Regions of the greatest Cα rmsd between the two structures are colored green (substrate-bound) and cyan (substrate-free). The red arrow denotes the direction of movement of Tyr81 from the substrate-bound to substrate-free form.

Received: May 31, 2013
Revised: July 5, 2013
Published: July 6, 2013

P450s but has two unique features. First, Asn242 replaces the highly conserved threonine found in the I helix of most other P450s. For P450cam, Thr252 is critical for the O_2-activation reaction[8,9] and is in position to interact directly with O_2. In P450cin, however, Asn242 does not appear to be critical for O_2 activation but instead is essential in regioselective hydroxylation.[10] Second, unlike P450cam, the active site is not surrounded by a wall of nonpolar residues but instead by an intricate lattice of water-bridged hydrogen bonds. This water network involves Tyr81, Asn242, and Asp241 (Figure 2). The

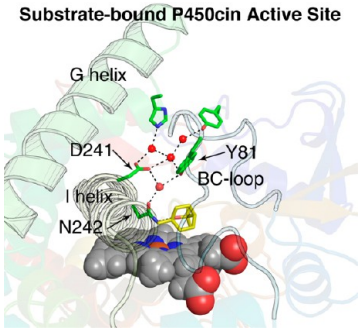

Figure 2. Substrate-bound P450cin active site with key residues colored green, waters colored red, and the ligand, cineole, colored yellow. The hydrogen-bond network is drawn with black dashes.

roles of Asn242 and Asp241 have been analyzed by mutagenesis, but the role of Tyr81 has not been explored. In addition, crystallographic data on these various mutants are limited. To probe further the unique water network in P450cin we have analyzed the Y81F and N242A mutants using crystallography, enzyme kinetics, titration calorimetry, and molecular dynamics.

MATERIALS AND METHODS

Site-Directed Mutagenesis. The pCW-P450cin expression plasmid with amino acids 2−7 deleted was provided by Prof. James De Voss. The Y81F and N242A mutants were cloned with overlapping complementary primers using a modification of the Invitrogen QuikChange site-directed mutagenesis protocol. Mutagenic primers with the mutated bases in bold are as follows: Y81F (f) 5′-GTG ACC TTC CCT CGC T**TC** GAA ACC GGC GAG TTC G-3′; Y81F (r) 5′-C GAA CTC GCC GGT TTC **GA**A GCG AGG GAA GGT CAC-3′; N242A (f) 5′-GCT TCT CGG CGG CAT CGA C**GC** CAC CGC ACG CTT CCT CAG-3′; N242A (r) 5′-CTG AGG AAG CGT GCG GTG **GC**G TCG ATG CCG CCG AGA AGC-3′. Each PCR reaction was split into two aliquots containing forward and reverse primers. Three PCR cycles with an annealing temperature of 59 °C were initiated for each aliquot. The reverse and forward reactions were then combined followed by 18 PCR cycles with an annealing temperature of 59 °C. DPN1 enzyme was added to the PCR reactions, and they were incubated for 5 h at 37 °C followed by chemical transformation into DH5*α E. coli*. Transformed DH5*α* were incubated overnight at 37 °C after they had been plated on Luria-Bertani broth agar plates containing 100 μg/mL of ampicillin. Plasmids were then prepared from overnight cultures and sequenced.

Catalytic Activity (NADPH Turnover). All activity assays were executed with a Cary 3E UV−vis spectrophotometer at room temperature. Catalytic rates were determined by using an established reconstituted turnover assay in which the native cindoxin reductase enzyme was replaced by *E.coli* flavodoxin reductase (Fpr).[11] NADPH provides reducing equivalents to Fpr for the sequential electron shuttling first to cindoxin (Cdx) and then to P450cin to hydroxylate 1,8-cineole to 1(*R*)-6*β*-hydroxycineole. The reaction contained 700 μL of 50 mM Tris buffer, pH 7.8, Fpr (4 μM), Cdx (4 μM), P450cin (0.5 μM), and 1,8-Cineole (200 μM). Catalytic turnover was initiated by adding NADPH (400 μM), and NADPH oxidation was determined from the loss of absorbance at 340 nm. The rate of NADPH consumption, corrected for background NADPH oxidation, was determined by dividing the slope of the curve by the NADPH extinction coefficient of 6.22 mM^{-1} cm^{-1}.[12] The reactions were incubated for 2 min, producing a linear curve. The k_{cat} value was determined by dividing the rate of NADPH consumption by the number of micromoles of P450cin used.

Product Formation (GC−MS). NADPH-driven catalytic turnover was initiated as described above. The samples taken at time intervals between 0 and 2 min were quenched and extracted with 700 μL of ethyl acetate. These samples were vortexed for 15 s followed by the addition of 4.6 μL of 30 μM camphor as an internal standard and vortexing again for 1 min. After centrifugation for 1 min, the organic layer was removed for gas chromatography−mass spectrometry analysis on a Finnigan Trace GC 2000 (Thermoquest Instruments) fitted with a J&W DB-5 column (30 m × 0.25 mm i.d.) (Agilent). Figure S1 displays the total ion current at selected time points for the WT, Y81F, and N242A mutants. The temperature was increased from 50 to 250 °C at a rate of 10 °C/min. A standard curve was generated by performing the same reaction in the absence of NADPH and adding known concentrations of cineole. All enzyme reactions were performed in triplicate. The ratio of the integrated peaks for cineole was divided by that of the internal standard and compared to the standard curve constructed from known cineole concentrations (Figure S2). Cineole and camphor, purchased from Sigma-Aldrich at greater than 98% purity, were assigned to peaks in the mass spectra consistent with their molecular weights. The peaks for gas chromatography−mass spectrometry m/z were 154 (M^+, 3.4%), 139 (M − CH_3), 108, 96, 93, 84, 81, 71, 69, 68, 58 for cineole and 152 (M^+, 4.1%), 137 (M − CH_3), 108, 95, 83, 81, 69, 67, 55 for camphor. A peak that increased with assay time had a mass spectrum previously reported for hydroxycineole and its fragments[13] (gas chromatography−mass spectrometry m/z: 170 (M^+, 0.62%), 155 (M − CH_3), 126, 111, 108, 93, 71, 69).

1,8-Cineole-Binding Spin-Shift Assays. Difference spectroscopy was used to determine the spin-shift binding constant, K_s, using previously published methods.[13] The assays were performed with a Cary 3E UV−vis spectrophotometer in the dual beam mode. Both the reference and sample cuvettes contained 1 mL of 2 μM P450cin diluted in 50 mM Tris, pH 7.8. The samples contained increasing concentrations of cineole diluted from a stock in the same buffer. The K_s value was determined by plotting the change in absorbance between high spin (392 nm) and low spin (415 nm) versus cineole concentration.

Isothermal Titration Calorimetry. Calorimetry measurements were performed with a VP-ITC titration calorimeter instrument from G.E. Healthcare. Protein samples were exchanged into 50 mM Tris, pH 7.8, by either gel filtration chromatography using Superdex 200 (G.E. Life Sciences) or by dialyzing with a $^1/_{1000}$ ratio of buffer multiple times. All samples

dx.doi.org/10.1021/bi4006946 | *Biochemistry* 2013, 52, 5039−5050

were extensively degassed under vacuum. Because the substrate is volatile, the buffer was purged of oxygen by bubbling with N_2 and degassed under a vacuum manifold prior to diluting the substrate into buffer at a $^1/_{600}$ ratio. The sample cell was filled with 220−290 μM of wild-type or N242A P450cin, whereas the Y81F mutant concentration was 430−450 μM. The injection syringe contained 10 mM cineole, and all experiments were performed in triplicate at 25 °C. Experiments were performed using 30−45 injections with a reference power of 10 μcal/sec, a stirring speed of 307 rpm, and a 150 s (WT/N242A) or 240 s (Y81F) time delay between injections. The injection volumes for the WT and N242A mutant consisted of 3 μL each. The injection volumes for the Y81F mutant were adjusted to 4 μL for the first two and the last four injections, and all other injection volumes were 15 μL. The heat values recorded were integrated, and the data were fit to a one-to-one binding mode.[14] Thermodynamic parameters were calculated with the Origin 7.0 graphing software. Standard deviations presented here are the result of three separate experiments and do not represent the standard deviations calculated from each individual curve fit.

Hydrogen Peroxide-Dependent Heme-Depletion Assays. Hydrogen peroxide-dependent heme-depletion assays were performed as described previously[15] with the following changes. Hydrogen peroxide and P450cin were incubated in 50 mM Tris buffer, pH 7.8, for 2 min with final concentrations of 100 mM and 7 μM, respectively. The loss of absorbance at 392 (WT) or 416 nm (mutant and substrate-free) were measured with a Cary 3E UV−vis spectrophotometer at room temperature. The fraction remaining was calculated as the ratio of the current absorbance to the starting absorbance. The assay was performed at increasing concentrations of cineole, and the rate of degradation was taken from the initial 30 s in which the slopes were linear.

Molecular Dynamics Simulations. The X-ray crystal structures solved herein were used as the starting configurations for each of the molecular dynamics simulations. Hydrogen atoms were added to both the protein and the crystallographic waters using the psfgen plugin with VMD 1.9.1 in preparation for the simulation.[16] To simulate bulk solvent, a water box with a 15 Å cushion in *x*, *y*, and *z* from the protein surface was added using VMD to generate the full system. The resulting systems of a corresponding size and number of atoms were then ready for study: P450CIN WT (73.4 × 93.18 × 93.14, 57 680 atoms) and P450CIN N242A (99.0 × 93.0 × 83.0, 71 245 atoms). The difference in the box size between the two systems was due to the protein being in different orientations with regards to the axis for each simulation.

All simulations were completed on Stampede (stampede.tacc.utexas.edu) using NAMD 2.9.[17] The CHARMM22 protein force field[18] was employed for all simulations along with the additional heme parameters that were available with the latest distribution of CHARMM force fields using the TIP3 water model. The cysteine−Fe (heme) bond was added with parameters from the previous P450 simulations.[19] Simulations were carried out at a constant temperature utilizing a Langevin thermostat,[20] the SHAKE algorithm[21] to constrain the bond lengths involving hydrogens, and a time step of 1.0 fs. The partial-mesh Ewald method was implemented in the calculations of the Coulomb interactions. Each system was allowed to minimize for 1000 steps before the simulation was allowed to proceed. Simulations were carried out for a minimum of 75 ns for each system, and the resulting trajectories were analyzed on local systems using VMD, Caver3.0,[22] Fpocket,[23] MDpocket,[24] and locally developed analysis tools.

An additional force field was produced for cineole for these simulations. Because cineole is very similar to the molecular structure of camphor that has previously been parametrized, the initial force field was based on a camphor force field developed previously.[25] The bonds unique to cineole were then constructed from similar parameters released in the latest CHARMM force-field release. The resulting force field was then compared to both the crystal structure and DFT calculations to ensure that there were no major penalties found in minimization as well as a control force field generated using the generalized small-molecule force field through paramchem.org.[26−28] The resulting force field that was found to reflect the accompanying DFT calculations (not shown) is included in the Supporting Information (Figure S3). The results were validated against previously obtained Amber force fields for cineole used in a separate simulation that further validated the obtained CHARMM cineole and protein force fields.

Caver and MDpocket Analysis. The resulting molecular dynamics trajectories were compressed, containing every 100th frame for an output rate of 100 ps/snapshot. Snapshots were converted to PDB files and fed into Caver3.0 and MDpocket for analysis. For Caver, a shell radius of 3 Å was used to define regions of bulk solvent, and a shell depth of 2 Å was used to minimize superficial tunnels near the protein surface. The probe radius was set to 1.2 Å and defines the minimum bottleneck radius a tunnel must exhibit to be identified. This probe radius was used for visualizing discrete tunnel pathways formed at some point in the simulation. To analyze the trend of a predominant tunnel over every snapshot, it was necessary to use a probe radius that is smaller than the smallest tunnel radius for any given snapshot. Therefore, a 1.0 Å probe radius was used for creating plots and tables that represent the single predominant tunnel present throughout the simulation. The starting-point atoms from which the channels were probed in the N242A mutant were the Ala241 Cβ, Fe, and cineole ethereal oxygen atoms. Attempts were made to use similar starting points for WT, but because the active site is much tighter than in the mutant, the starting point radius was smaller than the probe radius, prohibiting tunnel visualization. Therefore, we chose the Leu237 Cγ, Fe, and Asn242 Cα atoms to define our WT starting radius. For MDpocket analysis, the His176 side-chain dihedral angle fluctuated between a cutoff of −180° and +180°, making a plot in Cartesian coordinates misleading. Therefore, we wrapped the dihedral angle to produce continuous plots as described previously by Hollingsworth and Karplus.[29]

Protein Characterization. P450cin WT and mutant protein preparations had an A_{280}/A_{415} ratio between 1.2 and 1.3 in the absence of substrate. Protein concentrations were determined by using an ε_{415} of 150 mM^{-1} cm^{-1} for substrate-free protein.[13] WT and mutant proteins exhibited a shift in absorbance to 450 nm upon reduction and bubbling CO in excess substrate, which is characteristic of cytochrome P450 enzymes. Heme content was calculated to be >98% using the alkaline pyridine hemochromogen assay and an ε_{red557} of 34.7 mM^{-1} cm^{-1}.[30]

P450cin Purification and Crystallization. WT and mutant P450cin was expressed and purified as previously described[7] unless otherwise noted. The N242A and Y81F mutants were grown at 80 rpm and ambient temperature for 36

dx.doi.org/10.1021/bi4006946 | Biochemistry 2013, 52, 5039−5050

Table 1. Crystallographic Data and Refinement Statistics

data set	Y81F-3 mM cineole	Y81F-7 mM cineole	N242A
radiation source	Saturn 944	ALS BL 8.2.1	SSRL BL 9-2
space group	*P*212121	*P*212121	*P*21
unit cell dimensions (a, b, c) (Å)	60.46, 103.71, 127.59	68.81, 103.77, 127.71	64.43, 68.17, 103.71 β = 95.15°
resolution range (Å) (highest shell)	50.34−2.14 (2.22−2.14)	34.75−1.37 (1.45−1.37)	46.68−1.38 (1.45−1.38)
wavelength (Å)	1.54	1.00	0.98
total observations	215 793	783 177	483 599
unique reflections (highest shell)	50 211 (4797)	185 316 (27 034)	181 964 (26 082)
completeness (%) (highest shell)	98.3(95.5)	97.4 (94.9)	99.5 (98.3)
R_{sym} (highest shell)	0.081 (0.257)	0.070 (0.472)	0.061 (0.354)
$\langle I/\sigma \rangle$ (highest shell)	19.7 (4.22)	9.5 (2.0)	16.9 (1.9)
redundancy (highest shell)	4.3 (2.9)	4.2(3.3)	2.7 (2.2)
B factor, Wilson plot (Å^2)	27.3	15.0	13.7
unique reflections used in working set refinement	47 577	176 050	172 503
resolution range (Å) used in refinement	30.9−2.14	34.75−1.37	43.79−1.38
no. of protein atoms fit	6,336	6,336	6,334
no. of heteroatoms fit	143	142	145
no. of waters fit	472	970	1,202
R_{work} (%)	20.0	16.7	14.2
R_{free} (%)	26.3	20.7	17.8
rmsd bond length (Å)	0.012	0.008	0.014
rmsd bond angle	1.34	1.28	1.58

h prior to harvesting. One hundred micromolar δ-aminolevulinic acid was added upon induction and after 18 h. For the N242A mutant, the initial crystals were grown from a 1:1 ratio of 1 mM P450cin/well solution in sitting-drop vapor-diffusion Cryschem crystal trays (15% PEG 3350, 100 mM BisTris, pH 6.2, 150 mM lithium sulfate, 3−5 mM cineole, 3 mM TCEP-HCl, and 100 mM NaCl). For the Y81F mutant, it was necessary to increase the cineole concentration to 7 mM to obtain usable crystals, although we were able to obtain a small handful of high-quality crystals and one structure using 3 mM cineole. For the mutants, a 2 day incubation at room temperature produced crystals suitable for seeding. These crystals were then crushed to form a homogeneous seed stock followed by serial dilution in mother liquor. Crystals were grown in mother liquor containing 12% PEG 3350 and streak seeded after a 4 hr incubation at room temperature. A 5 day incubation at room temperature yielded crystals of sufficient quality for X-ray data collection. These crystals were transferred into a mother liquor solution containing 15% PEG 3350 and increasing concentrations of PEG400 to a final concentration of 30% before flash cooling and storage in liquid nitrogen.

P450cin N242A and Y81F Data Collection and Refinement. X-ray diffraction data for the P450cin N242A and Y81F mutants crystallized in 7 mM cineole were collected at the Stanford Synchrotron Radiation lightsource (Menlo Park, CA) on beamline 9-2 using a Mar325 CCD detector. The diffraction data for the Y81F mutant were collected at the Advanced Light Source (Berkeley, CA) on beamline 8.2.1. In each case, diffraction data were integrated using Mosflm[31] and scaled using SCALA[32] from the CCP4 suite.[33] For the N242A mutant, the initial 2mFo-DFc and Fo-Fc maps were calculated with FFT from the CCP4 suite using phases taken from the wild-type crystal structure (PDB ID IT2B). For the Y81F mutant, the initial maps were determined by molecular replacement in phaser using wild-type as a starting model. Refinement was carried out in Phenix.refine from the Phenix package.[34] For the N242A and Y81F data sets, individual coordinates were refined as well as anisotropic *B* factors. Iterative cycles of model improvement in Coot[35] followed by refinement resulted in our final refinement statistics (Table 1).

P450cin Y81F in 3 mM Cineole Data Collection and Refinement. Data for the Y81F mutant crystallized in 3 mM cineole were collected on an in-house Rigaku Micromax 007HF rotating anode and a Saturn 944 CCD detector. A stream of liquid nitrogen (Crystal Logic, Los Angeles, CA) kept the crystals at −160 C° during data collection. The crystal-to-detector distance was 100 mm, and the 2θ angle was −17°. The ω angle was incrementally increased by 0.5° with an exposure time of 45 s, giving a total of 360 frames per data scan in ω angle. Two data scans were collected at χ angles of 15 and 30°. The diffraction data were integrated, merged, and scaled using HKL2000.[36] The initial 2mFo-DFc and mFo-DFc maps were calculated with FFT from the CCP4 suite and phases from a higher-resolution Y81F crystal structure mentioned above (PDB ID 4LHT). *B* factors for individual atoms were refined isotropically and grouped for TLS refinement, and individual coordinates were refined using Phenix.refine. We were concerned about the possibility of model bias resulting from the initial poor 2Fo-Fc density for the cineole ligand. Therefore, we proceeded with two separate trials of refinement by omitting the cineole ligand in one approach and including it in the other. Similar refinement statistics were achieved in either case. Final refinement statistics were achieved through iterative cycles of model improvement in Coot and refinement in Phenix.refine.

RESULTS AND DISCUSSION

Substrate Binding. The Y81F mutant does not give a complete low-to-high-spin shift even at very high concentrations of cineole. As shown in Figure 3D, there is about a 50:50 mix of the low- and high-spin forms even at saturating levels of cineole. The WT enzyme, however, displays a single high-spin 392 nm peak at micromolar cineole concentrations (Figure 3B). It should be noted that previous work reported a 10-fold lower K_s than the one we obtained[10] (0.7 vs 5.5 μM). In these earlier studies, a quadratic model was used to fit the binding curve because the simplified model is not accurate

dx.doi.org/10.1021/bi4006946 | *Biochemistry* 2013, 52, 5039−5050

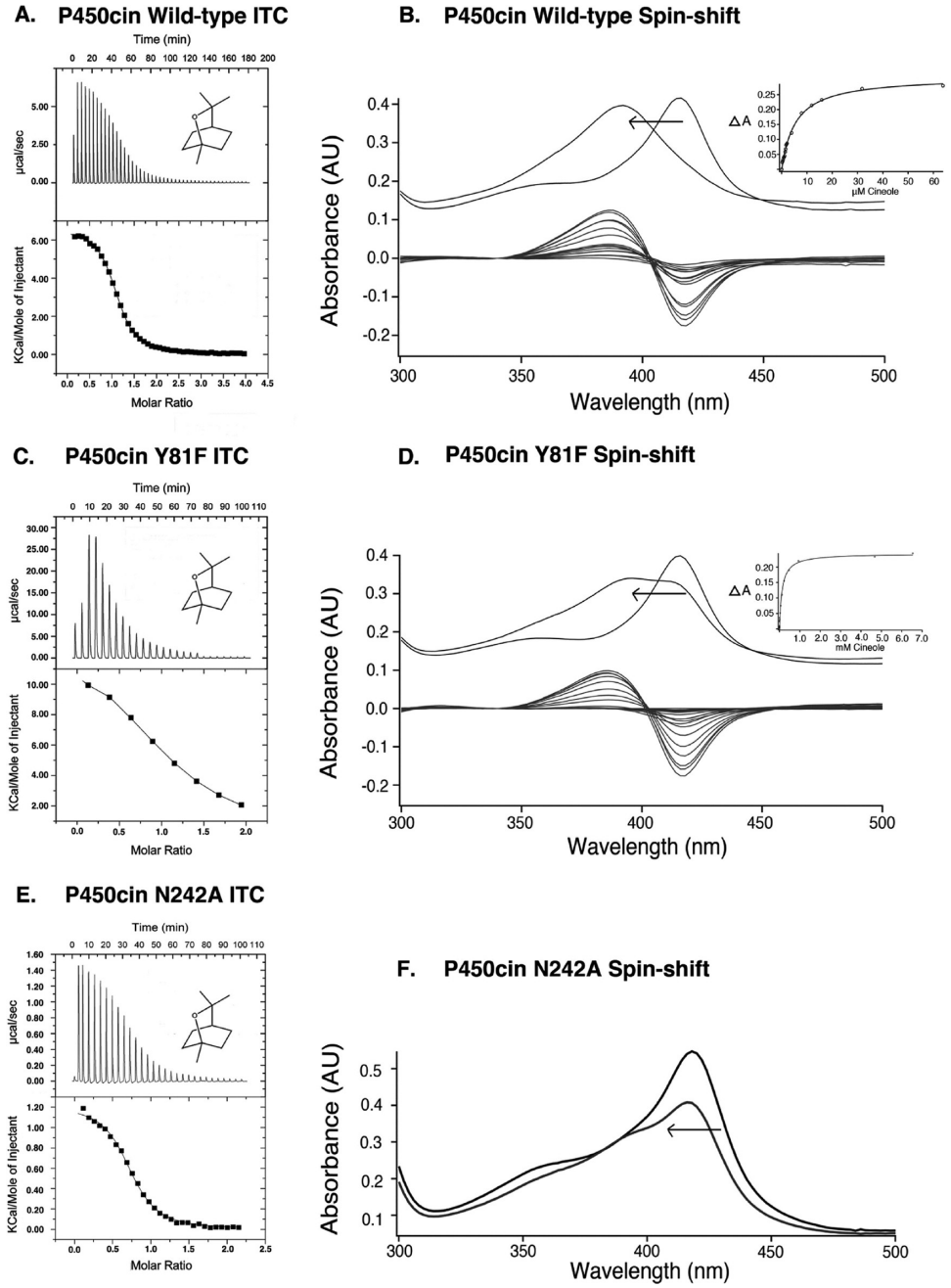

Figure 3. ITC binding isotherms and spectral binding assays for titrating ligand (cineole) into WT, Y81F, and N242A P450cin. Panels A, C, and E show the unintegrated heat exchange during each injection at the top and the integrated enthalpy as a function of the molar ratio of cineole to P450cin at the bottom. The curves were fit to a quadratic using a one-to-one binding model to obtain the thermodynamic parameters. Panels B and D depict the spectral binding assays for the WT enzyme and Y81F mutant. The starting and ending spectrum is shown above, with the arrow denoting the peak direction upon adding ligand. The difference in high spin (substrate bound, 393 nm) and low spin (substrate free, 415 nm) is plotted as a function of cineole concentration to give the spectral binding curve shown in the insets. Panel F does not contain a spectral binding curve because the peak-to-trough difference for the N242A mutant was too small to measure accurately.

Table 2. Enzymatic and Substrate-Binding Data

	k_{cat} (min^{-1})	product (min^{-1})	coupling (%)	K_s (μM)	K_d (μM)	ΔH (kcal mol^{-1})	$T\Delta S$ (kcal mol^{-1})	n-binding stochiometry
wild type	253 ± 5.4	248 ± 28.0	97.8	5.5	11.8 ± 0.21	6.90 ± 0.43	13.7 ± 0.43	1.04 ± 0.05
Y81F	166 ± 9.1	178 ± 15.8	105	125.2	161 ± 17.6	12.8 ± 1.00	18 ± 1.06	1.04 ± 0.04
N242A	79.6 ± 10.6	29.0 ± 3.0	36.4		12.6 ± 1.73	1.22 ± 0.02	7.89 ± 1.21	0.74 ± 0.08

when the K_s is less than the enzyme concentration. However, in our case, curve fitting using a simplified Michaelis–Menten approach resulted in the same binding constant as a quadratic model. For the Y81F mutant, K_s is 125 μM, which is about 20-fold higher than that for the WT enzyme (Table 2). As an independent method for estimating substrate binding, we

dx.doi.org/10.1021/bi4006946 | *Biochemistry* 2013, 52, 5039–5050

utilized isothermal titration calorimetry (ITC) to provide a spectrally independent K_d. ITC yields K_d values of 11.8 μM for WT (Figure 3A) and 161 μM for the Y81F mutant (Figure 3C), showing a similar trend to the spectrally determined K_s values (inset Figure 3B,D and Table 2).

The ITC results also show that for the WT enyzme substrate binding is enthalpically unfavorable by 7 kcal mol^{-1}; thus, it is entropically driven. The enthalpy and entropy contributions show a similar relationship for the Y81F and N242A mutants. Substrate-free P450 active sites have been shown to be highly solvated,[1,7,37] and the enthalpic penalty probably results from breaking water−water and water−protein hydrogen bonds upon substrate binding. The positive TΔS term provides supporting evidence of a conformational change that increases solvent entropy by burying exposed hydrophobic residues upon substrate binding, as suggested previously by ITC analysis of CYP130 ligand binding.[38]

The N242A mutant exhibits a very slight low-to-high-spin transition and was too small to confidently determine a K_s using UV−vis difference spectroscopy. ITC gives a K_d = 12.6 μM, which is close to the WT value of 11.8 μM (Table 2). The entropy contribution is also close to the WT value, whereas the enthalpy contribution is approximately $^1/_7$ that of WT. It is unlikely that this small difference is enough to account for loss of the cineole ethereal oxygen−Asn242 hydrogen bond. The reduction in enthalpy also makes sense if substrate binding in the N242A mutant does not expel water from the active site as it does in the WT enzyme because fewer hydrogen bonds would be disrupted upon substrate binding. The measured ΔG values are −6.7 and −6.8 kcal/mol for the N242A mutant and wild-type enzymes, respectively. This is in agreement with previous theoretical calulations where the N242A mutant results in only a modest change in binding affinity (0.1 to 0.5 kcal/mol).[10] Therefore, our data confirms that the N242A−cineole hydrogen bond contributes very little to the free energy of substrate binding.

Heme Accessibility, Spin State, and Enzyme Activity. The inability of the mutants to exhibit a full spin shift could be due to the open state dominating or water remaining coordinated to the heme iron in the closed state. We employed a hydrogen peroxide assay, previously used to measure P450 heme accessibility to small molecules,[15] to probe P450cin solvent accessibility. As shown in Figure 4, the wild-type heme is much less susceptible to H_2O_2 degradation in the substrate-bound closed state than the substrate-free open state, making this method a sensitive probe for the dominant conformation present in solution. Y81F is much more susceptible to heme degradation and much higher levels of substrate are required to protect the heme. In sharp contrast, N242A behaves similarly to WT at 1 mM substrate.

Although the Y81F mutant binds substrate more weakly, the substrate hydroxylation and coupling efficiency are near WT levels (Figure S2 and Table 2). The N242A mutant, however, has about 30% of the WT activity and is over 60% uncoupled, which is in agreement with previously published results.[10] In P450cam, substrate binding causes a rise in reduction potential such that electron transfer from its redox partner putidaredoxin becomes favorable.[39] It is likely that in the P450cin N242A mutant the reduced activity is a function of water coordinating the heme iron, giving a large low-spin population. This would result in a lowered redox potential where electron transfer from cindoxin does not occur. This phenomenon would also explain why the N242A mutant binds cineole as strongly as WT but

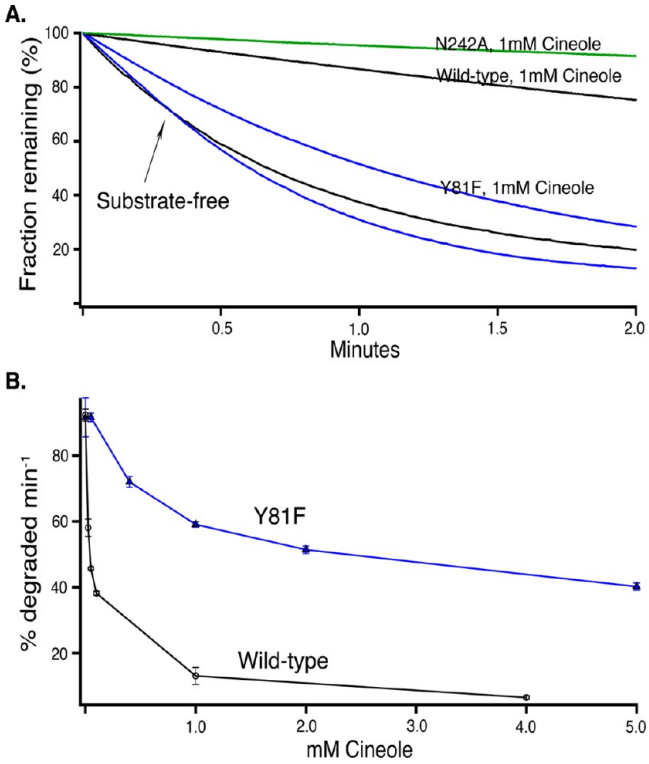

Figure 4. Effect of hydrogen peroxide on heme spectral properties. (A) 100 mM H_2O_2 was added at time 0 followed by monitoring the Soret peak at 392 nm for WT and the Y81F mutant. Absorbance at 415 nm was monitored for the N242A and substrate-free enzymes. A decrease in absorbance is due to heme destruction by H_2O_2 and provides an estimate of heme accessibility to H_2O_2. The fraction of the heme remaining for each enzyme was plotted over time. The curve for the N242A mutant is shown in green, and those for the Y81F mutant and WT are blue and black, respectively. (B) The percent heme degraded per minute was determined by plotting the initial slopes of the data from panel A versus increasing concentrations of cineole. The rates for WT and the Y81F mutant are plotted in blue and black, respectively.

gives very little spin shift. The crystal structure of a close homologue to P450cam, CYP101D2,[40] shows that the substrate can bind together with water coordinated to the heme iron giving a low-spin complex, but the substrate is not oriented correctly for regio- and stereoselective hydroxylation. In most P450−substrate complexes, the carbon atom to be hydroxylated is within 4 to 5 Å of the heme iron, which is a scenario that is not possible when water is coordinated to the heme. Therefore, there must be some active site adjustments that would allow for the simultaneous binding of both water and substrate. We have determined the crystal structures of the N242A and Y81F mutants to provide a structural underpinning for these possibilities and to explore how they relate to the active-site solvent structure.

Crystal Structures. To obtain crystals of the Y81F mutant, it was necessary to use higher concentrations of substrate (3 and 7 mM) than is required for WT which readily crystallizes in 1 mM cineole. 2mFo-DFc electron-density maps show that the crystals grown in 7 mM cineole exhibit greater density than those of the 3 mM structure, underscoring how poorly this mutant binds substrate (Figure 5C,D). The mutant Phe81 side chain is positioned similarly to the Tyr81 WT side chain, but there is a large change in the ordered water network. Water B,

dx.doi.org/10.1021/bi4006946 | Biochemistry 2013, 52, 5039−5050

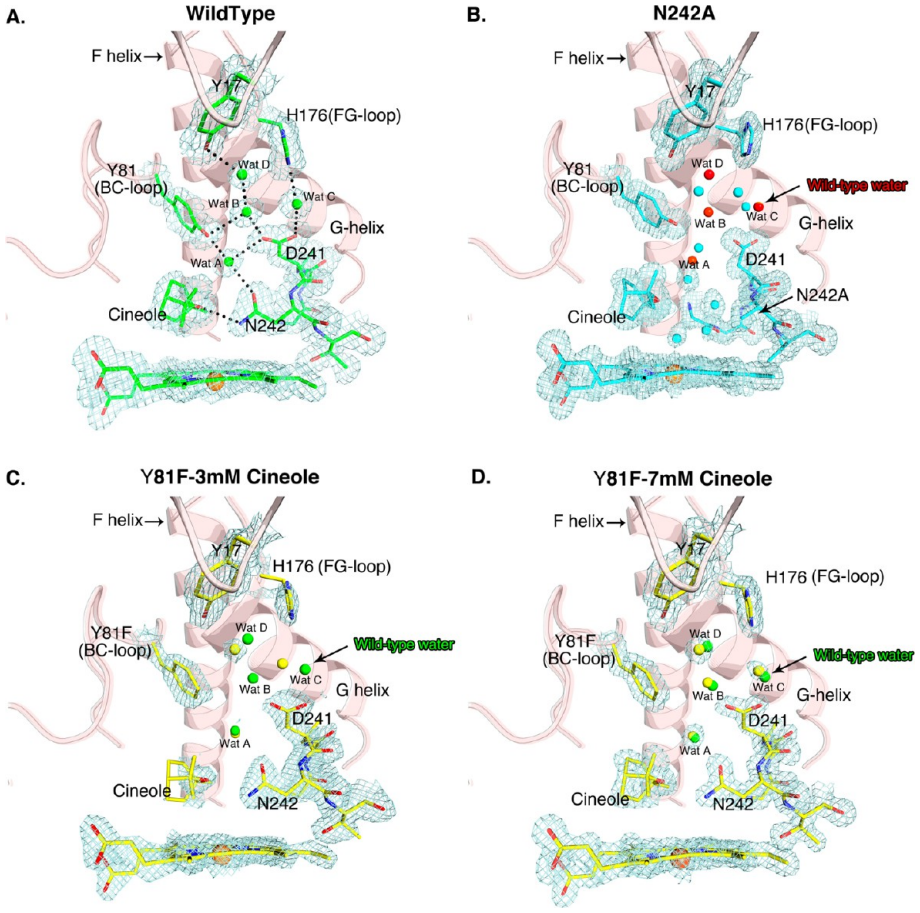

Figure 5. Active-site structures of WT and mutants. 2mFo-DFc maps were contoured to 1.7σ levels and shown for all atoms including water in the active site,with the exception of the N242A mutant. For the N242A mutant, the 2mFo-DFc maps were omitted for waters above the cineole ligand to compare clearly with the superimposed WT water in panel C. In panels B, C, and D, the WT water structure (red or green) has been superimposed over the N242A and Y81F active sites. The 2mFo-DFc-map signal for the Y81F mutant is too low to visualize the waters nearest the WT waters in A and C.

normally H-bonded to Tyr81, is clearly missing in the 3 mM structure and has poor density in the 7 mM structure. Water B is likely important because it provides a bridging H-bond from Tyr81 of the BC loop to the Asp241 residue of the I helix. At 335 and 328 Å^3, the volumes of the ligand-binding cavities determined for the structures in the 3 and 7 mM cineole mutants, respectively, are only slightly expanded compared to the wild type enzyme (300 Å^3) as calculated by fpocket.[23] However, given our earlier results, lower concentrations of cineole probably result in a more open active site that has been difficult to crystallize.

Because Asn242 and Tyr81 are tied together in the water-mediated H-bonded network, it was important to better understand the effect of the N242A mutant on the active-site water structure. Our earlier 3.05 Å structure[10] did not provide this type of detail, but we now have been able to solve the N242A structure to 1.3 Å. In addition, at 3.05 Å our previous map suggested an ambiguous substrate orientation. Unfortunately, it was not clear enough to interpret precisely how the substrate should be positioned. Our best guess was that multiple orientations were responsible for the observed electron density. However, at much higher resolution, it is evident that the substrate is clearly defined and oriented similar to that in WT P450cin. However, the smaller Ala242 side chain does allow the substrate to rotate slightly, moving closer to the I helix. The extra room provided by the smaller Ala242 side chain allows four more water molecules into the active site where one of them is 2.3 Å away from the heme iron (Figure 5B). This water may contribute to the inability of this mutant to produce a significant spin shift in solution. One of the new waters is H-bonded to Gly238, and there is a loss of the water B- and water C-bridged H-bond between Asp241of the I helix and both Tyr81 of the BC loop and H176 of the FG loop. The N242A mutant, therefore, breaks a water network that connects the I helix to the BC and FG loops. It is also interesting to note that these regions undergo the largest change in the closed/open transition. The increased solvation in the N242A mutant may also be responsible for the uncoupling observed for this enzyme.

The loss of a hydrogen bond between Asn242 and the substrate allows the I helix to corkscrew so that Asp241 can no longer hydrogen bond with waters B and C. This movement also allows His176 to retract, pulling the FG loop away from the active site. The net effect is that the distance between Asp241 and Tyr81 is no longer sufficient to entirely close off the active site from solvent. In Figure 6, a surface cutaway representation depicts a new solvent-accessible tunnel leading directly to the heme iron as calculated by Caver.[22] This tunnel traverses a pore created in the N242A mutant. In Figure 6B, we see a clear view to the active site waters in the N242A mutant as opposed to the wild-type enzyme that has a closed active site. In Figure 6C, we can see that the distance between Asp241 and

dx.doi.org/10.1021/bi4006946 | *Biochemistry* 2013, 52, 5039−5050

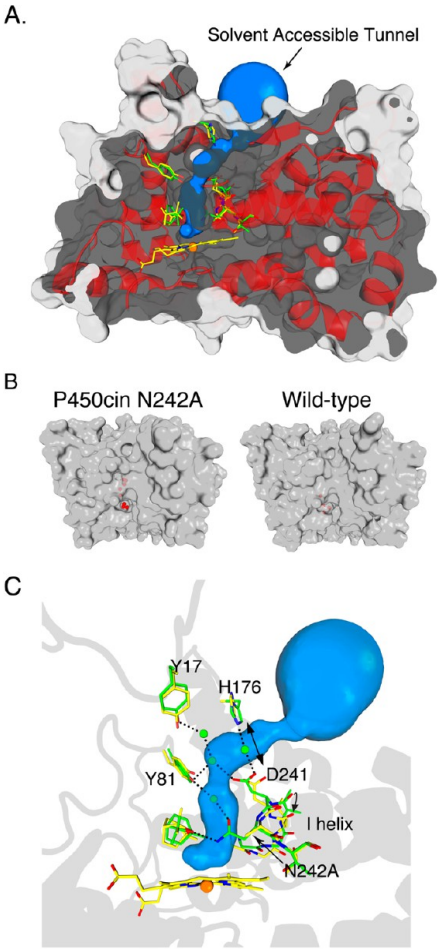

Figure 6. Cross section of the P450cin N242A mutant. (A) The surface is colored gray, and the backbone is drawn as a red ribbon. Active-site residues are colored yellow and green for N242A and WT P450cin, respectively. The solvent-accessible tunnel, calculated and visualized by the Pymol Caver 2.0 plugin, is shown in blue. (B) Surface representations are depicted for the N242A mutant on the left and WT on the right. Active-site waters are colored red. (C) Close-up of the active site, with WT residues shown as green sticks superimposed over N242A residues colored yellow.

His176 has increased from 4.9 to 6.8 Å, leaving a pore above the active site. The Asp241 movement is associated with the corkscrewing of the I-helix backbone that also opens up the active site pocket, increasing the volume from approximately 300 to 446 Å^3 as calculated by fpocket.[23] The 146 Å^3 difference is much larger than the difference in area between the Ala and Asn side chains, suggesting that the I-helix movement results in an enlarged ligand-binding pocket. An in silico mutation of N242A to Asn confirms this observation, giving a pocket size of 407 Å^3. This suggests that the N242A mutant causes an increase of about 100 Å^3 in pocket size that is not due to the void left by removal of the Asn side chain.

In the N242A mutant, the pocket is now bound by F-helix Thr175 rather than the Tyr81−His176 water-bridged pair (Figure 7). Because uncoupling is often associated with a disruption in the proper proton-delivery machinery, the large room and additional solvent very near the O_2 binding site in N242A probably accounts for the 60% uncoupling in N242A. Even so, as noted earlier Asn242 is not as critical for activity as is Thr252 in P450cam. This is most likely because Thr252 in P450cam directly participates in the H-bonded network

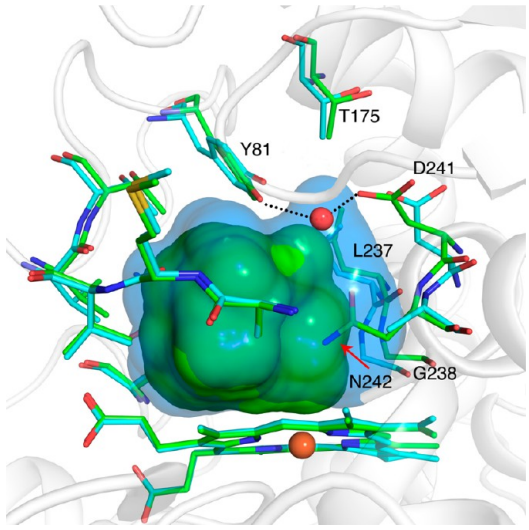

Figure 7. Surface representation of the active-site pockets for wild-type (green) superimposed over the N242A mutant (cyan). The Y81−N241 water-bridged H-bond is shown in red, with black dashes denoting hydrogen bonding.

required for proper proton delivery to dioxygen, whereas the main role of Asn242 is to hold the substrate in place for regioselective hydroxylation.[10]

Molecular Dynamics Simulations. Molecular dynamics have provided important insights into solvent channels as well as the dynamic properties of active-site hydration in P450 enzymes.[41−43] We studied the effect of active-site water movement in WT and the N242A mutant by carrying out 75 ns MD simulations. The WT enzyme exhibited no water entering the active-site pocket throughout the 75 ns simulation, whereas the N242A mutant harbored water in its binding pocket a majority of the time. Given the analysis of the N242A and wild-type crystal structures earlier, it was tempting to implicate the His176−Asp241 water bridge as the key factor in the differences in solvent accessibility between the two enzymes. Analysis of the molecular dynamics simulations, however, paints a different picture.

Evolving solvent-accessible channels were tracked during the course of the simulation using Caver3.0[22] and MDpocket.[24] The distance between the His176 nitrogen and the Asp241 β-carbon does not correlate with the solvent-accessible channels formed during the simulation. Rather, it correlates perfectly with the side-chain dihedral angles of the His176 side chain (Figure 8B). His176 points toward the active site for almost half of the simulation whereupon it rotates about the Cα−Cβ bond by over 100°, with the two dihedral planes defined by N−Cα−Cβ and Cγ−Cα−N. Contrary to our expectations, a change in the His176 dihedral angle does not cause a solvent-accessible channel to form during the course of the simulation. In Figure 8C, the bottleneck radius of the highest scoring channel is plotted as a function of time for N242A in blue with a yellow trend line and for the WT enzyme in black with a red trend line. The shaded area defines the values of the tunnel-bottleneck radii that are less than 1.4 Å, which are not large enough to allow solvent passage. N242A and the wild-type enzyme possess channels with bottleneck radii of 1.52 and 1.41 Å, respectively, regardless of the His176 dihedral angle. In the inset of Figure 8C, we can see examples of solvent channels in WT P450cin with H176 in either orientation. It appears that the wild-type enzyme makes subtle adjustments, allowing room

dx.doi.org/10.1021/bi4006946 | *Biochemistry* 2013, 52, 5039−5050

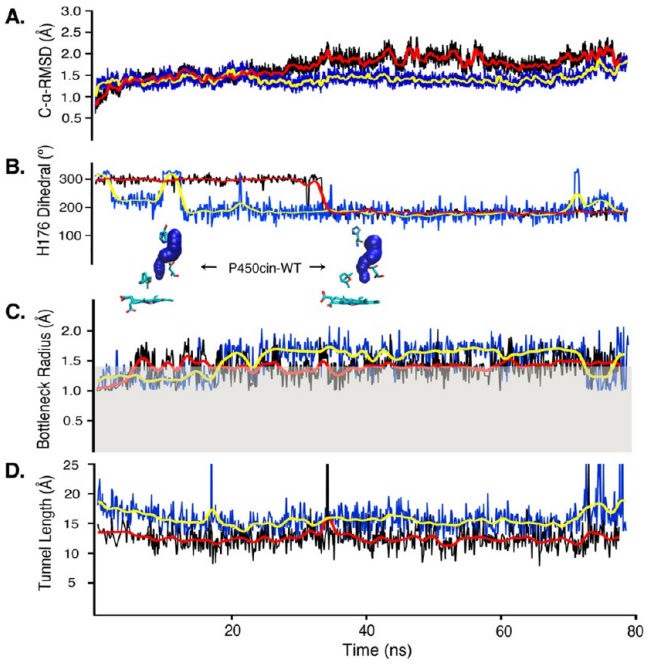

Figure 8. Analysis of the molecular dynamics trajectories, with WT in black (red trend line) and the N242A mutant in blue (yellow trend line). (A) Cα rmsd of the WT and mutant enzymes are plotted vs time. (B) H176 side-chain dihedral angle defined by the N−Cα−Cβ and Cγ−Cα−N planes is plotted over time. (C) Average bottleneck radius of tunnels clustered into tunnel 1 were calculated by Caver3.0 and plotted over the trajectory with a cutoff of 1.0 Å. The gray area represents all bottleneck radii less than 1.4 Å. (D) Tunnel length of the solvent-accessible channels with bottleneck radii greater than 1.2 Å were plotted over the trajectory.

for a solvent-accessible tunnel to form between H176 and D241 regardless of their orientation.

The main difference between the evolving tunnels in WT and the N242A mutant is the tunnel-path length. The N242A mutant has an average tunnel length of 15.7 Å, which is more than 3 Å longer than WT that has a length of 12.5 Å (Figure 8D). In Figure 9, tunnels with bottleneck radii greater than 1.2 Å are visualized for WT and the N242A mutant throughout the simulation. The tunnels form three major clusters: tunnel 1a (blue), 1b (yellow), and tunnel 2 (red) where both tunnels 1b and 2 are offshoots of 1a. In WT, none of these tunnels traversed from the surface to the heme iron. This lack of solvent penetration is due to a narrowing of the active site in the WT enzyme. The tunnels have no problem accessing the N242A heme iron and travel over 3 Å further into the active site.

Asn242 undoubtedly acts as a plug to keep the channel from entering the active site. However, its hydrogen bond with the substrate has the added function of tightening up the ligand-binding pocket. As mentioned earlier, the N242A mutant results in a translation of the I helix that enlarges the active-site pocket by over 100 Å^3 when compared to that of the wild type, as visualized in Figure 10. This enlargement is far more than can be accounted for by the N242 side chain alone and is maintained over the course of the MD simulations. The increased size of the active-site pocket occurs on the I-helix side, which is probably because of the helix movement discussed earlier. It is important to point out that because P450cin likely undergoes a structural change upon oxygen binding[5,6] we cannot make predictions about solvent

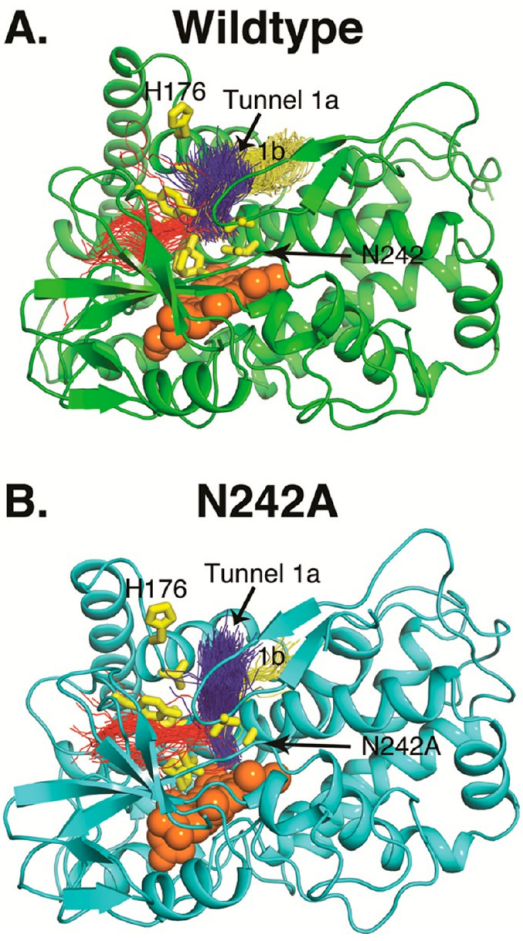

Figure 9. Center lines of individual solvent-accessible tunnels are shown, as calculated by Caver3.0, with a bottleneck radius cutoff of 1.2 Å. The top three scoring tunnels after clustering were colored blue, yellow, and red respectively. Each line represents a solvent-accessible tunnel appearing at some point in the MD simulation.

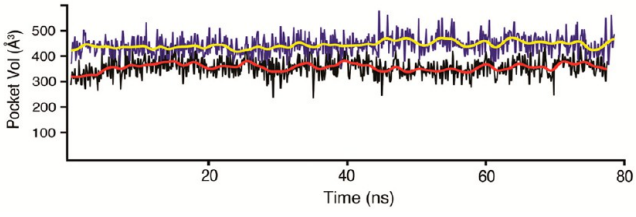

Figure 10. Analysis of WT and the N242A mutant active-site pocket volumes calculated by MDpocket over the molecular dynamics trajectories. WT (black with red trend line) and the N242A mutant (blue with yellow trend line) are plotted against time. The analysis shown here was performed every 0.1 ns for a total simulation time of 75 ns.

accessibility during oxygen activation. However, we can say that the Asn242 residue helps to constrict the active site, keeping water out before catalysis begins.

CONCLUSIONS

Although P450 enzyme active sites are predominately hydrophobic, many Fe(III)-substrate-bound crystal structures contain ordered waters near the active site. Much work has gone into understanding the role of water, from examining its fundamental structural roles to its participation in proton-

dx.doi.org/10.1021/bi4006946 | *Biochemistry* 2013, 52, 5039−5050

relay networks, particularly in P450cam.[5,6,44−48] Unfortunately, changes in the active-site structure and water during oxygen activation have made these assignments more difficult in cases where an Fe(II)−O_2 complex structure is not available. Here, we have found critical roles for two water molecules near the Fe(III) P450cin active site. First, the H-bond between water B and Tyr81 is critical to maintain substrate binding. The Y81F mutant results in a large increase in solvent accessibility, suggesting the predominance of a more open conformation. Thus, the removal of just one H-bonding group from the active-site water network dramatically decreases substrate binding by shifting the conformational equilibrium to the open state. This observation underscores the delicate energetic balance between the open and closed states. Second, we have also found that the Asn242 residue, occurring at a catalytically critical position in other P450s, plays a role in restricting solvent accessibility to the active site. The N242A mutant disrupts a delicate relationship between the enzyme pocket volume and the ability to exclude excess water, preventing P450cin from converting to the high-spin state. Specifically, N242A, lacking the Asn242−cineole and Asn242−water A H-bonds, causes a shift in the I helix that disrupts the ordered water network and loosens the ligand-binding pocket. This finding may explain why previously published Asn242 mutants show reduced catalytic activity and at least 30% uncoupling.[49] From these results, we conclude that an active-site lattice of protein−water H-bonds is important for substrate binding, active-site hydration, and controlling the open/closed transition, which are all critically important to enzyme function.

■ ASSOCIATED CONTENT

Ⓢ Supporting Information

Total GC−MS ion counts for selected time points in the extraction of cineole from the NADPH turnover assay for WT, Y81F, and N242A mutants plotted against retention time, GC−MS peak areas from the total ion counts for cineole divided by the peak areas for the internal standard, CHARMM compatible cineole force field. This material is available free of charge via the Internet at http://pubs.acs.org.

Accession Codes

Coordinates and structure factors have been deposited in the Protein Data Bank under accession numbers 4LHT, 4L6G, and 4L77.

■ AUTHOR INFORMATION

Corresponding Author

*E-mail: poulos@uci.edu. Phone: 949-824-7020.

Funding

This work was supported by NIH grant GM33688.

Funding

Y.M. acknowledges the National Science Foundation for predoctoral fellowship support. S.A.H. was supported by an institutional cancer biology training grant (NIH/NCI T32CA009054).

Notes

The authors declare no competing financial interest.

■ ACKNOWLEDGMENTS

We thank the University of California, Irvine Department of Chemistry mass spectrometry facility and especially Drs. John Greaves and Beniam Berhane for help with troubleshooting experiments as well as mass spec specialist Shirin Sorooshian for her dedication in maintaining the instrumentation. This Article involves research carried out at the Stanford Synchrotron Radiation Laboratory, a national user facility operated by Stanford University on behalf of the U.S. Department of Energy, Office of Basic Energy Sciences. The SSRL Structural Molecular Biology Program is supported by the Department of Energy, Office of Biological and Environmental Research and by the National Institutes of Health, National Center for Research Resources, Biomedical Technology Program, and the National Institute of General Medical Sciences. We also acknowledge the Advanced Light Source supported by the Director, Office of Science, Office of Basic Energy Sciences, of the U.S. Department of Energy under contract no. DE-AC02-05CH11231.

■ ABBREVIATIONS

CYP, cytochrome P450; CO, carbon monoxide; Cdx, cindoxin; CN^-, cyanide; DEAE, diethylaminoethyl cellulose; DEER, double electron−electron resonance; DTT, dithiothreitol; EPR, electron paramagnetic resonance; ENDOR, electron nuclear double resonance; IPTG, isopropyl β-D-1-thiogalactopyranoside; MD, molecular dynamics; NADH, nicotinamide adenine dinucleotide; ITC, isothermal titration calorimetry; NADPH, nicotinamide adenine dinucleotide phosphate; NMR, nuclear magnetic resonance; PCR, polymerase chain reaction; PEG, poly(ethylene glycol); PMSF, phenylmethylsulfonyl fluoride; rmsd, root-mean-square deviation; SDS-PAGE, sodium dodecyl sulfate polyacrylamide gel electrophoresis; Tris, tris(hydroxymethyl)aminomethane; VMD, visual molecular dynamics; WT, wild type

■ REFERENCES

(1) Lee, Y. T., Wilson, R. F., Rupniewski, I., and Goodin, D. B. (2010) P450cam visits an open conformation in the absence of substrate. *Biochemistry 49*, 3412−3419.

(2) Lee, Y. T., Glazer, E. C., Wilson, R. F., Stout, C. D., and Goodin, D. B. (2011) Three clusters of conformational states in p450cam reveal a multistep pathway for closing of the substrate access channel. *Biochemistry 50*, 693−703.

(3) Stoll, S., Lee, Y. T., Zhang, M., Wilson, R. F., Britt, R. D., and Goodin, D. B. (2012) Double electron-electron resonance shows cytochrome P450cam undergoes a conformational change in solution upon binding substrate. *Proc. Natl. Acad. Sci. U.S.A. 109*, 12888−12893.

(4) Miao, Y., Yi, Z., Cantrell, C., Glass, D. C., Baudry, J., Jain, N., and Smith, J. C. (2012) Coupled flexibility change in cytochrome P450cam substrate binding determined by neutron scattering, NMR, and molecular dynamics simulation. *Biophys. J. 103*, 2167−2176.

(5) Nagano, S., Cupp-Vickery, J. R., and Poulos, T. L. (2005) Crystal structures of the ferrous dioxygen complex of wild-type cytochrome P450eryF and its mutants, A245S and A245T - Investigation of the proton transfer system in P450eryF. *J. Biol. Chem. 280*, 22102−22107.

(6) Schlichting, I., Berendzen, J., Chu, K., Stock, A. M., Maves, S. A., Benson, D. E., Sweet, R. M., Ringe, D., Petsko, G. A., and Sligar, S. G. (2000) The catalytic pathway of cytochrome p450cam at atomic resolution. *Science 287*, 1615−1622.

(7) Madrona, Y., Tripathi, S., Li, H., and Poulos, T. L. (2012) Crystal structures of substrate-free and nitrosyl cytochrome P450cin: implications for O(2) activation. *Biochemistry 51*, 6623−6631.

(8) Imai, M., Shimada, H., Watanabe, Y., Matsushima-Hibiya, Y., Makino, R., Koga, H., Horiuchi, T., and Ishimura, Y. (1989) Uncoupling of the cytochrome P-450cam monooxygenase reaction by a single mutation, threonine-252 to alanine or valine: possible role of the hydroxy amino acid in oxygen activation. *Proc. Natl. Acad. Sci. U.S.A. 86*, 7823−7827.

(9) Martinis, S. A., Atkins, W. M., Stayton, P. S., and Sligar, S. G. (1989) A conserved residue of cytochrome P-450 is involved in heme-oxygen stability and activation. *J. Am. Chem. Soc. 111*, 9252−9253.
(10) Meharenna, Y. T., Slessor, K. E., Cavaignac, S. M., Poulos, T. L., and De Voss, J. J. (2008) The critical role of substrate-protein hydrogen bonding in the control of regioselective hydroxylation in p450cin. *J. Biol. Chem. 283*, 10804−10812.
(11) Hawkes, D. B., Slessor, K. E., Bernhardt, P. V., and De Voss, J. J. (2010) Cloning, expression and purification of cindoxin, an unusual Fmn-containing cytochrome p450 redox partner. *ChemBioChem 11*, 1107−1114.
(12) Bergmeyer, H. U. (1975) New values for the molar extinction coefficients of NADH and NADPH for the use in routine laboratories (author's translation). *Z. Klin. Chem. Klin. Biochem. 13*, 507−508.
(13) Hawkes, D. B., Adams, G. W., Burlingame, A. L., Ortiz de Montellano, P. R., and De Voss, J. J. (2002) Cytochrome P450cin (CYP176A), Isolation, expression, and characterization. *J. Biol. Chem. 277*, 27725−27732.
(14) Pierce, M. M., Raman, C. S., and Nall, B. T. (1999) Isothermal titration calorimetry of protein-protein interactions. *Methods 19*, 213−221.
(15) Sineva, E. V., and Davydov, D. R. (2010) Constrained water access to the active site of cytochrome P450 from the piezophilic bacterium Photobacterium profundum. *High Pressure Res. 30*, 466−474.
(16) Humphrey, W., Dalke, A., and Schulten, K. (1996) VMD: visual molecular dynamics. *J. Mol. Graphics 14*, 27−38.
(17) Phillips, J. C., Braun, R., Wang, W., Gumbart, J., Tajkhorshid, E., Villa, E., Chipot, C., Skeel, R. D., Kale, L., and Schulten, K. (2005) Scalable molecular dynamics with NAMD. *J. Comput. Chem. 26*, 1781−1802.
(18) Brooks, B. R., Brooks, C. L., 3rd, Mackerell, A. D., Jr., Nilsson, L., Petrella, R. J., Roux, B., Won, Y., Archontis, G., Bartels, C., Boresch, S., Caflisch, A., Caves, L., Cui, Q., Dinner, A. R., Feig, M., Fischer, S., Gao, J., Hodoscek, M., Im, W., Kuczera, K., Lazaridis, T., Ma, J., Ovchinnikov, V., Paci, E., Pastor, R. W., Post, C. B., Pu, J. Z., Schaefer, M., Tidor, B., Venable, R. M., Woodcock, H. L., Wu, X., Yang, W., York, D. M., and Karplus, M. (2009) CHARMM: The biomolecular simulation program. *J. Comput. Chem. 30*, 1545−1614.
(19) Shahrokh, K., Orendt, A., Yost, G. S., and Cheatham, T. E., 3rd (2012) Quantum mechanically derived AMBER-compatible heme parameters for various states of the cytochrome P450 catalytic cycle. *J. Comput. Chem. 33*, 119−133.
(20) Martyna, G. J., Tobias, D. J., and Klein, M. L. (1994) Constant-pressure molecular-dynamics algorithms. *J. Chem. Phys. 101*, 4177−4189.
(21) Ryckaert, J.-P., Ciccotti, G., and Berendsen, H. J. C. (1977) Numerical integration of the Cartesian equations of motion of a system with constraints: molecular dynamics of n-alkanes. *J. Comput. Phys. 23*, 327−341.
(22) Chovancova, E., Pavelka, A., Benes, P., Strnad, O., Brezovsky, J., Kozlikova, B., Gora, A., Sustr, V., Klvana, M., Medek, P., Biedermannova, L., Sochor, J., and Damborsky, J. (2012) CAVER 3.0: a tool for the analysis of transport pathways in dynamic protein structures. *PLoS Comput. Biol. 8*, e1002708-1−e1002708-12.
(23) Le Guilloux, V., Schmidtke, P., and Tuffery, P. (2009) Fpocket: An open source platform for ligand pocket detection. *BMC Bioinf. 10*, 168.
(24) Schmidtke, P., Bidon-Chanal, A., Luque, F. J., and Barril, X. (2011) MDpocket: Open-source cavity detection and characterization on molecular dynamics trajectories. *Bioinformatics 27*, 3276−3285.
(25) Schoneboom, J. C., Lin, H., Reuter, N., Thiel, W., Cohen, S., Ogliaro, F., and Shaik, S. (2002) The elusive oxidant species of cytochrome P450 enzymes: characterization by combined quantum mechanical/molecular mechanical (QM/MM) calculations. *J. Am. Chem. Soc. 124*, 8142−8151.
(26) Vanommeslaeghe, K., Hatcher, E., Acharya, C., Kundu, S., Zhong, S., Shim, J., Darian, E., Guvench, O., Lopes, P., Vorobyov, I., and Mackerell, A. D., Jr. (2010) CHARMM general force field: A force field for drug-like molecules compatible with the CHARMM all-atom additive biological force fields. *J. Comput. Chem. 31*, 671−690.
(27) Vanommeslaeghe, K., and MacKerell, A. D., Jr. (2012) Automation of the CHARMM general force field (CGenFF) I: Bond perception and atom typing. *J. Chem. Inf. Model. 52*, 3144−3154.
(28) Vanommeslaeghe, K., Raman, E. P., and MacKerell, A. D., Jr. (2012) Automation of the CHARMM general force field (CGenFF) II: Assignment of bonded parameters and partial atomic charges. *J. Chem. Inf. Model 52*, 3155−3168.
(29) Hollingsworth, S. A., and Karplus, P. A. (2010) A fresh look at the Ramachandran plot and the occurrence of standard structures in proteins. *Biomol. Concepts 1*, 271−283.
(30) Berry, E. A., and Trumpower, B. L. (1987) Simultaneous determination of hemes a, b, and c from pyridine hemochrome spectra. *Anal. Biochem. 161*, 1−15.
(31) Leslie, A. G. W., Powell, H. R. (2007) Processing diffraction data with mosflm, in *Evolving Methods for Macromolecular Crystallography* (Read, R. J., Sussman, J. L., Eds.) pp 41−51, Springer Verlag, Dordrecht, The Netherlands.
(32) Kabsch, W. (1988) Evaluation of single-crystal X-ray-diffraction data from a position-sensitive detector. *J. Appl. Crystallogr. 21*, 916−924.
(33) Winn, M. D., Ballard, C. C., Cowtan, K. D., Dodson, E. J., Emsley, P., Evans, P. R., Keegan, R. M., Krissinel, E. B., Leslie, A. G., McCoy, A., McNicholas, S. J., Murshudov, G. N., Pannu, N. S., Potterton, E. A., Powell, H. R., Read, R. J., Vagin, A., and Wilson, K. S. (2011) Overview of the CCP4 suite and current developments. *Acta Crystallogr., Sect. D 67*, 235−242.
(34) Adams, P. D., Afonine, P. V., Bunkoczi, G., Chen, V. B., Davis, I. W., Echols, N., Headd, J. J., Hung, L. W., Kapral, G. J., Grosse-Kunstleve, R. W., McCoy, A. J., Moriarty, N. W., Oeffner, R., Read, R. J., Richardson, D. C., Richardson, J. S., Terwilliger, T. C., and Zwart, P. H. (2010) PHENIX: A comprehensive Python-based system for macromolecular structure solution. *Acta Crystallogr., Sect. D 66*, 213−221.
(35) Emsley, P., and Cowtan, K. (2004) Coot: Model-building tools for molecular graphics. *Acta Crystallogr., Sect. D 60*, 2126−2132.
(36) Otwinowski, Z., and Minor, W. (1997) Processing of X-ray diffraction data collected in oscillation mode. *Methods Enzymol. 276*, 307−326.
(37) Mast, N., White, M. A., Bjorkhem, I., Johnson, E. F., Stout, C. D., and Pikuleva, I. A. (2008) Crystal structures of substrate-bound and substrate-free cytochrome P450 46A1, the principal cholesterol hydroxylase in the brain. *Proc. Natl. Acad. Sci. U.S.A. 105*, 9546−9551.
(38) Ouellet, H., Podust, L. M., and de Montellano, P. R. (2008) Mycobacterium tuberculosis CYP130: Crystal structure, biophysical characterization, and interactions with antifungal azole drugs. *J. Biol. Chem. 283*, 5069−5080.
(39) Sligar, S. G., and Gunsalus, I. C. (1976) Thermodynamic model of regulation - modulation of redox equilibria in camphor monoxygenase. *Proc. Natl. Acad. Sci. U.S.A. 73*, 1078−1082.
(40) Yang, W., Bell, S. G., Wang, H., Zhou, W., Bartlam, M., Wong, L. L., and Rao, Z. (2011) The structure of CYP101D2 unveils a potential path for substrate entry into the active site. *Biochem. J. 433*, 85−93.
(41) Cojocaru, V., Winn, P. J., and Wade, R. C. (2007) The ins and outs of cytochrome P450s. *Biochim. Biophys. Acta 1770*, 390−401.
(42) Hendrychova, T., Berka, K., Navratilova, V., Anzenbacher, P., and Otyepka, M. (2012) Dynamics and hydration of the active sites of mammalian cytochromes P450 probed by molecular dynamics simulations. *Curr. Drug Metab. 13*, 177−189.
(43) Rydberg, P., Rod, T. H., Olsen, L., and Ryde, U. (2007) Dynamics of water molecules in the active-site cavity of human cytochromes P450. *J. Phys. Chem. B 111*, 5445−5457.
(44) Haines, D. C., Tomchick, D. R., Machius, M., and Peterson, J. A. (2001) Pivotal role of water in the mechanism of P450BM-3. *Biochemistry 40*, 13456−13465.

(45) Kumar, D., Altun, A., Shaikh, S., and Thiel, W. (2011) Water as biocatalyst in cytochrome P450. *Faraday Discuss. 148*, 373−383 . See the general discussion in the same issue, pp 421−441.
(46) Nagano, S., and Poulos, T. L. (2005) Crystallographic study on the dioxygen complex of wild-type and mutant cytochrome P450cam. Implications for the dioxygen activation mechanism. *J. Biol. Chem. 280*, 31659−31663.
(47) Raag, R., Martinis, S. A., Sligar, S. G., and Poulos, T. L. (1991) Crystal structure of the cytochrome P-450CAM active site mutant Thr252Ala. *Biochemistry 30*, 11420−11429.
(48) Vidakovic, M., Sligar, S. G., Li, H., and Poulos, T. L. (1998) Understanding the role of the essential Asp251 in cytochrome p450cam using site-directed mutagenesis, crystallography, and kinetic solvent isotope effect. *Biochemistry 37*, 9211−9219.
(49) Slessor, K. E., Farlow, A. J., Cavaignac, S. M., Stok, J. E., and De Voss, J. J. (2011) Oxygen activation by P450(cin): Protein and substrate mutagenesis. *Arch. Biochem. Biophys. 507*, 154−162.